RSC Advances

PAPER

View Article Online
View Journal | View Issue

Open Access Article. Published on 24 January 2019. Downloaded on 1/12/2026 1:20:46 PM.
This article is licensed under a Creative Commons Attribution-NonCommercial 3.0 Unported Licence.

Check for updates

Cite this: *RSC Adv.*, 2019, **9**, 3303

Mn^{4+}-activated $BaLaMgSbO_6$ double-perovskite phosphor: a novel high-efficiency far-red-emitting luminescent material for indoor plant growth lighting

Qi Sun, Shaoying Wang, Balaji Devakumar, Liangling Sun, Jia Liang and Xiaoyong Huang *

Received 3rd December 2018
Accepted 18th January 2019

DOI: 10.1039/c8ra09928f

rsc.li/rsc-advances

In the present work, novel high-efficiency Mn^{4+}-activated $BaLaMgSbO_6$ (BLMS) far-red-emitting phosphors used for plant growth LEDs were successfully synthesized *via* a solid-state reaction method. X-ray diffraction (XRD), photoluminescence (PL), temperature-dependent PL, CIE color coordinates, and lifetimes as well as internal quantum efficiency (IQE) were used to characterize the phosphor samples. The excitation spectrum of the as-obtained BLMS:Mn^{4+} phosphors presented two wide bands covering 250–550 nm and the emission spectrum exhibited a far-red emission band in the range of 650–800 nm peaked at 700 nm. Concentration-dependent PL properties of BLMS:Mn^{4+} phosphors were studied. The optimal doping concentration of Mn^{4+} ions was 0.6 mol%, and the concentration quenching mechanism was determined to be the nonradiative energy transfer among the nearest-neighbor Mn^{4+} activators. Impressively, the BLMS:0.6%Mn^{4+} sample showed an outstanding IQE of 83%. In addition, luminescence thermal quenching characteristics were also analyzed. Furthermore, the PL spectrum of BLMS:0.6%Mn^{4+} sample was compared with the absorption spectrum of phytochrome P_{FR}. Finally, after combining BLMS:0.6%Mn^{4+} phosphors with a 365 nm near-UV LED chip, a far-red light-emitting diode (LED) device was successfully achieved to demonstrate its possible applications in plant growth LEDs.

1. Introduction

Recently, red-emitting luminescent materials doped with rare-earth ions (such as Eu^{3+}, Eu^{2+}, Ce^{3+}) and transitional metal ions (such as Mn^{4+} and Cr^{3+}) have attracted much attention due to their promising applications in lighting and displays.[1–14] Mn^{4+} ion with a $3d^3$ electron configuration belongs to the transitional metal ion, and in recent years Mn^{4+}-activated red-emitting phosphors have been widely reported for warm-white light-emitting diodes (LEDs) towards general lighting applications.[15–19] Generally, Mn^{4+} ions can substitute for W^{6+}, Sn^{4+}, Sb^{5+}, Al^{3+}, Ge^{4+}, Ta^{5+}, and Ti^{4+} ions in the octahedral or distorted octahedral systems.[20–30] Just recently, Mn^{4+} doped oxide-based phosphors with excellent luminescent properties and chemical stability such as Li_2MgZrO_4:Mn^{4+}, $Ca_3La_2W_2O_{12}$:Mn^{4+}, and $La(MgTi)_{1/2}O_3$:Mn^{4+} have been researched for their potential applications in far-red LEDs for indoor plant growth.[31–33] It is known that far-red light around 730 nm (700–740 nm) is most needed for photosynthesis in all plant growth, especially the growth of plant stems.[34,35] The perovskite-type compounds are potential hosts for luminescent materials due to their excellent optical properties and diversity of their structure and composition.[36–44] Therefore, double perovskite $BaLaMgSbO_6$ (BLMS), which contains many [SbO_6] octahedrons, would be a novel good host for doping Mn^{4+} ions.

In this work, highly efficient BLMS:Mn^{4+} far-red-emitting phosphors were synthesized by a high-temperature solid-state reaction method in air atmosphere. Upon 340 nm excitation, BLMS:Mn^{4+} phosphors gave a far-red emission band between 650 and 800 nm with a maximum peak at 700 nm, which matched well with the absorption band of phytochrome P_{FR}. The optimal Mn^{4+} ions doping concentration was about 0.6 mol%, for which the BLMS:Mn^{4+} phosphors exhibited the highest luminescence intensity. The full width at half maximum (FWHM) and CIE chromaticity coordinates of BLMS:0.6%Mn^{4+} sample were ~38 nm and (0.7231, 0.2768), respectively. More importantly, when excited at 340 nm, the BLMS:0.6%Mn^{4+} sample had internal quantum efficiency (IQE) as high as 83%. These results suggested that the BLMS:Mn^{4+} could be considered as promising far-red-emitting phosphors for application in far-red LEDs towards indoor plant growth lighting.

College of Physics and Optoelectronics, Taiyuan University of Technology, Taiyuan 030024, P. R. China. E-mail: huangxy04@126.com

Open Access Article. Published on 24 January 2019. Downloaded on 1/12/2026 1:20:46 PM.
This article is licensed under a Creative Commons Attribution-NonCommercial 3.0 Unported Licence.

2. Experimental

A series of $BaLaMgSb_{1-x}O_6$:$x$$Mn^{4+}$ (BLMS:$x$$Mn^{4+}$; x = 0.2, 0.4, 0.6, 0.8, 1.0, and 1.2 mol%) phosphors were synthesized by using a high-temperature solid-state reaction method with $BaCO_3$ (analytical reagent, AR), La_2O_3 (99.99%), MgO (AR), Sb_2O_5 (AR), and $MnCO_3$ (AR) as starting raw materials. These materials were weighed based on the stoichiometric ratio and ground thoroughly in an agate mortar. The mixed mixtures were firstly heated at 600 °C for 3 h. Subsequently, they were reground and sintered again at 1500 °C for 6 h. Finally, the resulting products were cooled down to room temperature naturally and then ground once again to get the fine powders for further characterization.

The X-ray diffraction (XRD) patterns of the samples were identified using a Bruker D8 X-ray diffractometer with Cu Kα radiation (λ = 1.5406 Å). The photoluminescence (PL) and PL excitation (PLE) spectra as well as decay curves of the as-obtained phosphors were recorded on an Edinburgh FS5 spectrometer equipped with a 150 W continued-wavelength Xenon lamp and a pulsed Xenon lamp, respectively. The IQE was measured by using the Edinburgh FS5 spectrometer equipped with an integrating sphere coated with $BaSO_4$. The temperature-dependent PL spectra of the phosphors ranging from 303 to 463 K were recorded on the same spectrometer with a temperature controlling system.

3. Results and discussion

Fig. 1 shows the XRD patterns of BLMS:$x$$Mn^{4+}$ (x = 0.2%, 0.6%, 0.8%, and 1.2%) samples. All the observed diffraction peaks of the as-obtained samples were similar, suggesting that doping Mn^{4+} ions did not significantly influence the crystal structure. To further gain more structural information, the Rietveld refinement of BLMS:0.6%Mn^{4+} was conducted, as shown in Fig. 1(b). The cross shows the observed patterns, the red solid line indicates the calculated patterns, the green solid line refers to the background line, the blue line represents the difference between the experimental and calculated data, and short vertical pink line stands for the positions of Bragg reflection. Moreover, the refinement results demonstrated that the BLMS:0.6%Mn^{4+} belonged to a cubic system with space group $Fm\bar{3}m$. The lattice parameters were calculated to be $a = b = c$ = 8.04869 Å, $\alpha = \beta = \gamma = 90°$, V = 525.406 Å^3, and N = 4. The crystal structure of BLMS:0.6%Mn^{4+} was displayed in Fig. 1(c). Sb^{5+} and Mg^{2+} were surrounded by the six nearest-neighbor oxygen ligand ions, which formed [SbO_6] and [MgO_6] octahedrons. As well known, when Mn^{4+} ions entered into the octahedral sites, red emission might be observed. According to the difference of ionic radii (r (Mn^{4+}) = 0.53 Å, r (Sb^{5+}) = 0.60 Å, r (Mg^{2+}) = 0.72 Å, r (Ba^{2+}) = 1.35 Å, and r (La^{3+}) = 1.32 Å), so Mn^{4+} ions preferred to occupy the Sb^{5+} sites in BLMS host owing to their similar ionic radii.

Fig. 2(a) shows the PLE and PL spectra of BLMS:0.6%Mn^{4+} sample at room temperature. Monitored with a emission wavelength of 700 nm, the obtained PLE spectrum of BLMS:0.6%Mn^{4+} sample consisted of two wide bands covering 250–550 nm, which could be deconvoluted into three Gaussian component peaks at 336 nm, 383 nm, and 501 nm. The first strong band centered at 336 nm was assigned to the Mn–O charge transfer band (CTB) and the Mn^{4+} spin-allowed transitions of $^4A_{2g} \rightarrow {}^4T_{1g}$.[45] The second band centered at 383 nm was attributed to the spin-allowed transition of Mn^{4+}: $^4A_{2g} \rightarrow {}^2T_{2g}$.[46] The third band centered at 501 nm was due to the spin-allowed transition of Mn^{4+}: $^4A_{2g} \rightarrow {}^4T_{2g}$.[47] The broad excitation bands of BLMS phosphors located in the near-UV region, indicating that BLMN:Mn^{4+} were suitable to be used as far-red phosphors with efficient excitation of near-UV LED chips.[48,49] Upon 340 nm excitation, the obtained emission spectrum had a narrow emission band in the wavelength range of 650–800 nm peaking at 700 nm, which was attributed to the spin-forbidden $^2E_g \rightarrow {}^4A_{2g}$ transition of Mn^{4+}.[50–52] The full width at half maximum (FWHM) of the emission band was about 38 nm, which was narrower than that of $Ca_3La_2W_2O_{12}$:Mn^{4+} (FWHM: 39 nm), Li_2MgTiO_4:Mn^{4+} (FWHM: 46 nm), and $Na_2MgAl_{10}O_{17}$:Mn^{4+} (FWHM: 105 nm).[1,32,51]

The CIE chromaticity coordinates of BLMS:0.6%Mn^{4+} sample were calculated and illustrated in Fig. 2(b). The CIE coordinates of BLMS:0.6%Mn^{4+} were found to be (0.7231, 0.2768), which located near the edge of the CIE diagram. Obviously, BLMS:Mn^{4+} phosphors had the good CIE chromaticity coordinates, which were located in the far-red region. As shown in the inset of Fig. 2(b), the phosphors emitted bright red light under 365 nm UV light, which indicated that the

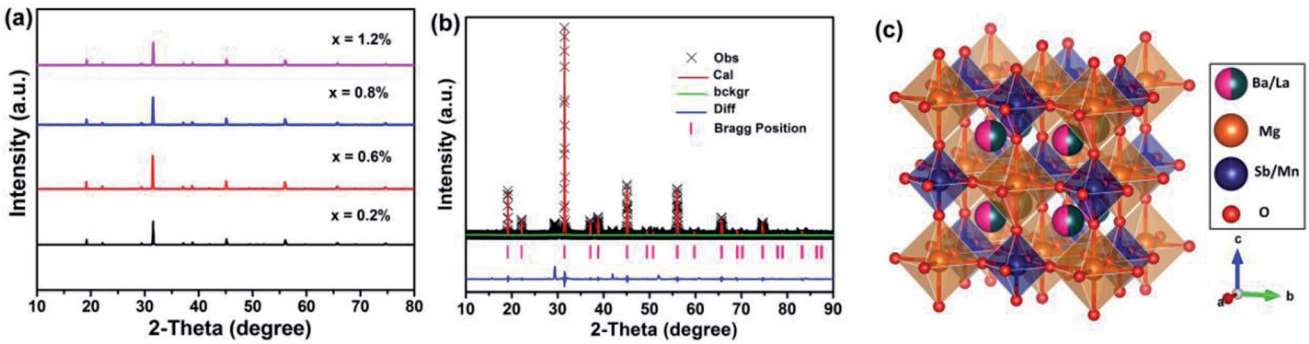

Fig. 1 (a) XRD patterns of BLMS:$x$$Mn^{4+}$ (x = 0.2%, 0.6%, 0.8% and 1.2%) phosphors. (b) Rietveld refinement XRD patterns of BLMS:0.6%Mn^{4+} phosphors. (c) The crystal structure of BLMS:0.6%Mn^{4+}.

Open Access Article. Published on 24 January 2019. Downloaded on 1/12/2026 1:20:46 PM.
This article is licensed under a Creative Commons Attribution-NonCommercial 3.0 Unported Licence.

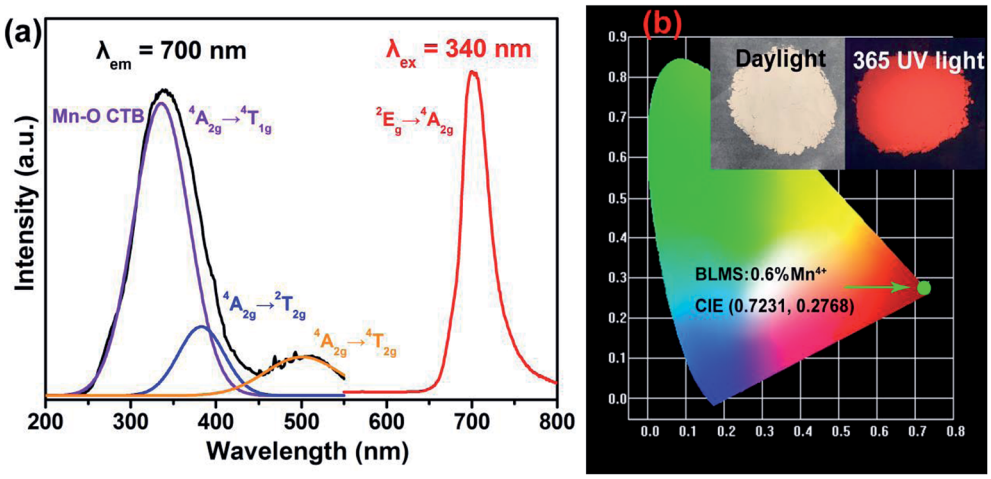

Fig. 2 (a) PLE and PL spectra of BLMS:0.6%Mn^{4+} phosphors. (b) CIE chromaticity coordinates of BLMS:0.6%Mn^{4+} phosphors under 340 nm excitation. The inset shows the digital photographs of BLMS:0.6%Mn^{4+} phosphors in daylight and under a 365 nm UV lamp.

BLMS:Mn^{4+} phosphors were remarkably suitable for indoor plant growth.

Fig. 3(a) shows the PL spectra of BLMS:Mn^{4+} phosphors with various Mn^{4+} doping concentrations. As depicted in Fig. 3(a), the shapes and positions of the emission spectra of all the samples were almost identical except for the emission intensities, which further proved that doping Mn^{4+} ions had little influence on crystal structure. As exhibited in Fig. 3(b), the emission intensity of this series of phosphors increased first and reached a maximum at $x = 0.6\%$, then decreased with

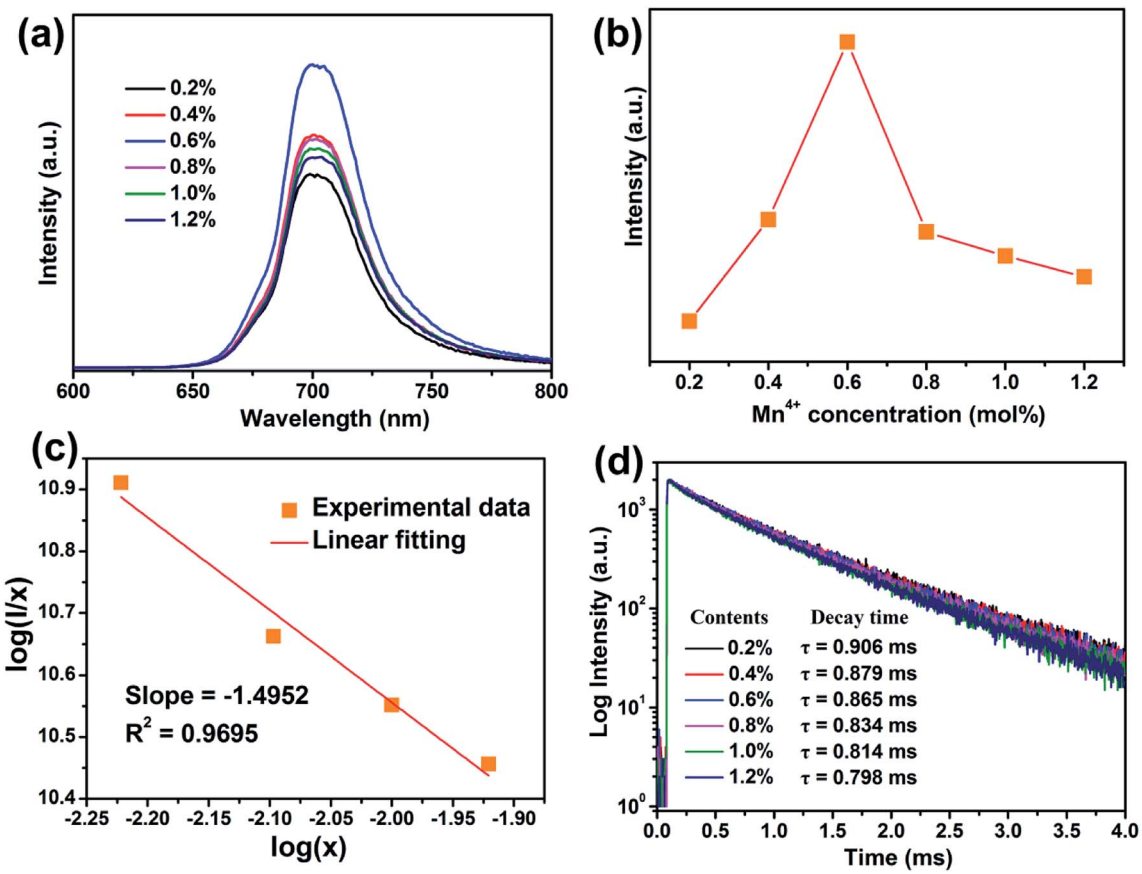

Fig. 3 (a) PL spectra of BLMS:xMn^{4+} (x = 0.2%, 0.4%, 0.6%, 0.8%, 1.0%, and 1.2%) phosphors under 340 nm excitation. (b) PL intensity of BLMS:xMn^{4+} as a function of Mn^{4+} doping concentration. (c) Linear fitting of log(x) *versus* log(I/x) in BLMS:xMn^{4+} phosphors excited at 340 nm. (d) Decay curves and calculated lifetimes of BLMS:xMn^{4+} (x = 0.2%, 0.4%, 0.6%, 0.8%, 1.0%, and 1.2%) under 340 nm excitation and monitored at 700 nm.

Open Access Article. Published on 24 January 2019. Downloaded on 1/12/2026 1:20:46 PM.
This article is licensed under a Creative Commons Attribution-NonCommercial 3.0 Unported Licence.

further increase in the Mn^{4+} concentration. This phenomenon was attributed to concentration quenching effect.[53] Concentration quenching is usually caused by the energy transfer within the nearest Mn^{4+} ions with the terminal step ending at a defect or killer site.[1,54] Since there was no overlap between PLE and PL spectra of BLMS:Mn^{4+}, so the radiation reabsorption was not dominant energy transfer mechanism. In order to figure out which mechanism was responsible for the concentration quenching among Mn^{4+} ions in the BLMS host, the critical distance (R_c) between Mn^{4+} ions was roughly calculated using the following equation:[55,56]

$$R_c \approx 2\left[\frac{3V}{4\pi X_c N}\right]^{1/3}, \quad (1)$$

where V is the volume of the host lattice, X_c refers to the critical doping concentration of Mn^{4+} ions, and N is the number of available sites for the dopant in the unit cell. In this work, the $X_c = 0.6\%$; $V = 525.406$ Å^3; and $N = 4$, respectively. Therefore, the calculated R_c value for Mn^{4+} was determined to be 34.71 Å, which was higher than 5 Å. Consequently, we inferred that the concentration quenching mainly took place *via* an electric multipolar interaction among Mn^{4+} ions. To further determine the type of interaction mechanism between Mn^{4+} ions, we could use the following equation:[57]

$$\frac{I}{x} = K\left[1+\beta(x)^{\theta/3}\right]^{-1} \quad (2)$$

where I is the emission intensity of BLMS:Mn^{4+} phosphors; x represents the Mn^{4+} concentration; K and β are the constants for the same excitation condition; and θ is an index of the electric multipolar character with $\theta = 3$, 6, 8 and 10 corresponding to the nonradiative energy transfer among the nearest-neighbor ions, dipole–dipole, dipole-quadrupole and quadrupole–quadrupole interactions, respectively.[58,59] The dependence of $\log(I/x)$ on $\log(x)$, as clearly displayed in Fig. 3(c), was well linearly fitted with a slope $(-\theta/3) = -1.4952$. Thus $\theta = 4.4856$, which was approximately calculated to be 3, implying that the major concentration quenching mechanism in BLMS:Mn^{4+} was the nonradiative energy transfer among the nearest-neighbor Mn^{4+} ions.[58–60]

Fig. 3(d) illustrates the room-temperature PL decay curves of the 700 nm emissions of BLMS:$x$$Mn^{4+}$ samples upon 340 nm excitation. All the decay curves could be well-fitted by using the following equation:[61]

$$I_t = A_1 \exp\left(-\frac{t}{\tau_1}\right) + A_2 \exp\left(-\frac{t}{\tau_2}\right) \quad (3)$$

where I_t is the luminescence intensities at time t; A_1 and A_2 represent constants; and τ_1 and τ_2 correspond to the short and

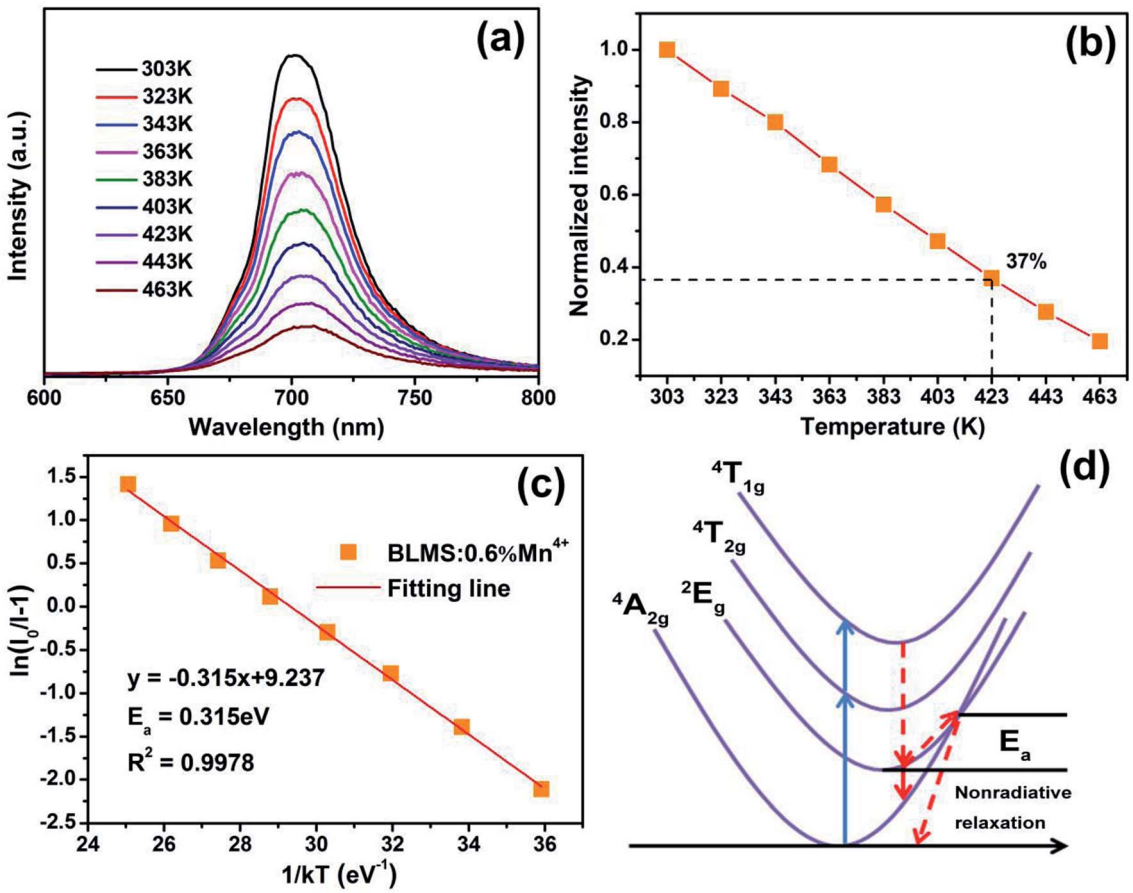

Fig. 4 (a) Temperature-dependent PL spectra of BLMS:0.6%Mn^{4+} phosphors under 340 nm excitation. (b) The normalized PL intensities of BLMS:0.6%Mn^{4+} phosphors at different temperature from 303 to 463 K. (c) The plot of $\ln(I_0/I - 1)$ *versus* $1/kT$ and the calculated activation energy (E_a) for the BLMS:0.6%Mn^{4+} phosphors. (d) The configuration coordinate diagram of Mn^{4+}.

Open Access Article. Published on 24 January 2019. Downloaded on 1/12/2026 1:20:46 PM.
This article is licensed under a Creative Commons Attribution-NonCommercial 3.0 Unported Licence.

long lifetimes for the exponential components, respectively. Furthermore, the average lifetime τ_s could be calculated by the following equation:[62]

$$\tau_s = (A_1\tau_1^2 + A_2\tau_2^2)/(A_1\tau_1 + A_2\tau_2) \quad (4)$$

The calculated lifetimes were also shown in Fig. 3(d). It was found that the luminescence lifetime decreased gradually from 0.906 to 0.798 ms with increasing Mn^{4+} concentrations, which was due to the increasing possibility of nonradiative energy migration among the adjacent Mn^{4+} ions.[27]

The temperature-dependent PL spectra of BLMS:0.6%Mn^{4+} phosphors under excitation at 340 nm were measured and illustrated in Fig. 4(a). Note that the emission profiles of BLMS:0.6%Mn^{4+} sample at different temperatures almost did not change except for PL intensity. It was clearly observed that the emission intensity decreased continuously with increasing temperature because of the thermal quenching effect. Fig. 4(b) shows the normalized PL intensity of the BLMS:0.6%Mn^{4+} phosphors as a function of temperature. The emission intensity at 423 K (150 °C) remained 37% of that at 303 K (30 °C). Moreover, the activation energy (E_a) was calculated *via* the equation, which is expressed as follows:[63,64]

$$\ln\left(\frac{I_0}{I} - 1\right) = \ln A - \frac{E_a}{kT} \quad (5)$$

where I_0 and I represent the emission intensity of the BLMS:0.6%Mn^{4+} phosphor at room temperature and at different given temperatures T, respectively; k is the Boltzmann coefficient; A is the constant; and E_a is activation energy. According to the linear relationship between $\ln(I_0/I - 1)$ and $1/kT$, which was plotted in Fig. 4(c), the value of E_a was obtained to be 0.315 eV. The relatively high E_a demonstrated that the as-obtained phosphors had good thermal stability.

The thermal quenching mechanism of BLMS:Mn^{4+} could be explained by the configuration coordinate scheme, as illustrated in Fig. 4(d). When the electrons at ground state $^4A_{2g}$ absorbed energy, they would be pumped to the excited states of $^4T_{1g}$ and $^4T_{2g}$, and then they could relax to the lowest excited state ^2E_g through nonradiative transition (red dashed line). After that they returned to the ground states $^4A_{2g}$ by radiative transition (red solid line), which emitted far-red light. However, when the temperature was elevated, a partial electrons at ^2E_g state were more likely to be thermally excited *via* the cross point between $^4A_{2g}$ and ^2E_g states, and could finally transit to the ground state with nonradiative transition, leading to lower the

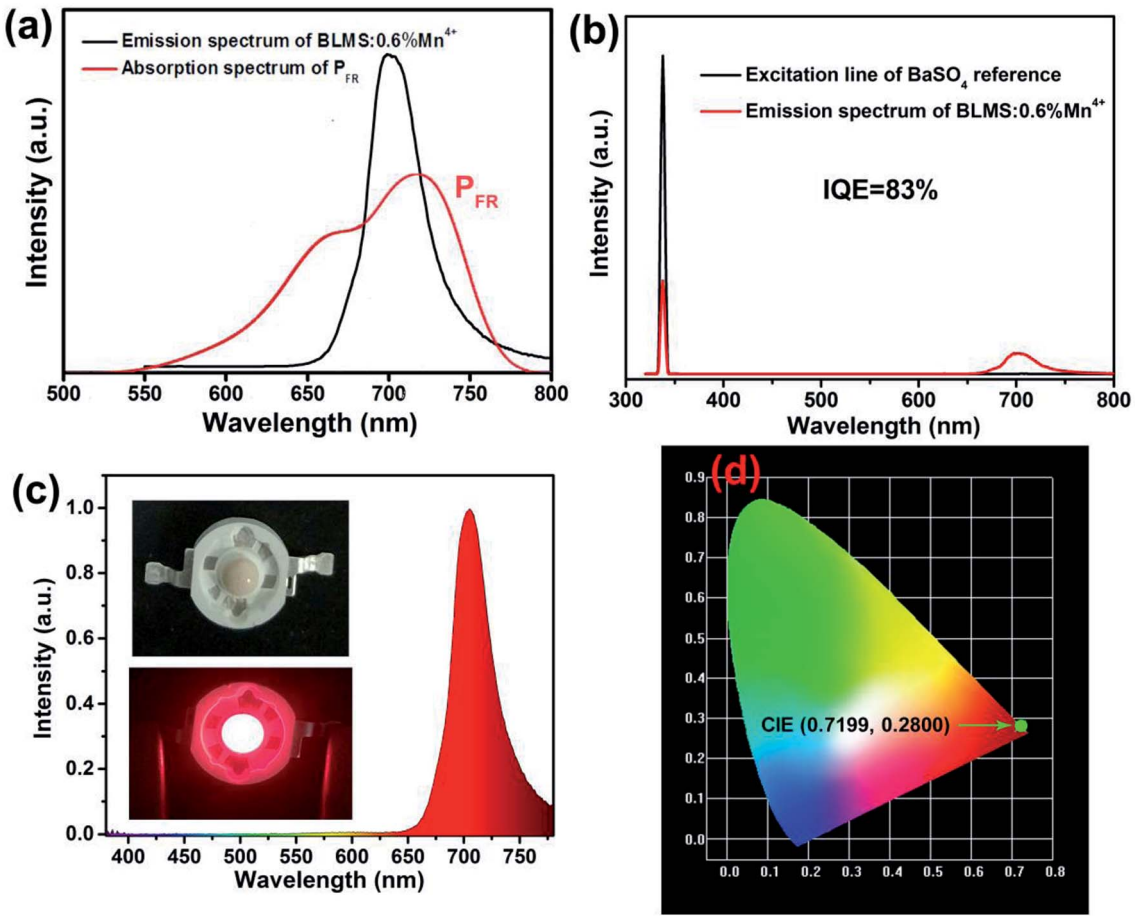

Fig. 5 (a) PL spectrum of BLMS:0.6%Mn^{4+} phosphors and the absorption spectrum of phytochrome P_{FR}. (b) Excitation line of $BaSO_4$ and the PL spectrum of BLMS:0.6%Mn^{4+} phosphor collected using an integrating sphere. (c) EL spectrum of the fabricated far-red LED device by using BLMS:0.6%Mn^{4+} phosphors and a 365 nm near-UV LED chip under a driven current of 120 mA. Inset shows the fabricated LED device and corresponding luminescent image. (d) CIE chromaticity coordinates of the far-red LED device.

Open Access Article. Published on 24 January 2019. Downloaded on 1/12/2026 1:20:46 PM.
This article is licensed under a Creative Commons Attribution-NonCommercial 3.0 Unported Licence.

Table 1 Comparison of several reported Mn^{4+}-activated red-emitting phosphors for indoor plant growth LEDs

Hosts	Concentrations	PLE peak (nm)	PL peak (nm)	IQE	Ref.
Li_2MgZrO_4	0.4%	335	670	32.3%	31
$Sr_9Y_2W_4O_{24}$	0.5%	366	680	49.8%	67
Ca_2LaSbO_6	0.5%	354	687	52.2%	68
$CaYMgSbO_6$	0.2%	294	688	51.5%	69
Sr_3NaSbO_6	0.5%	320	695	56.2%	70
Ca_2LaTaO_6	0.4%	325	696	34.6%	71
Gd_2ZnTiO_6	0.2%	365	705	39.7%	26
$La(MgTi)_{1/2}O_3$	0.8%	345	708	27.2%	33
$SrGdAlO_4$	0.1%	353	709	23%	72
$Ca_3La_2W_2O_{12}$	0.8%	360	711	47.9%	32
$Ca_{14}Al_{10}Zn_6O_{35}$	0.5%	467	713	19.4%	73
$LiLaMgWO_6$	0.7%	344	713	69.1%	65
$CaGdAlO_4$	0.2%	349	715	45%	29
$BaLaMgSbO_6$	0.6%	340	700	83%	This work

luminescence efficiency, which was so-called thermal quenching.[54]

Fig. 5(a) shows the PL spectrum of BLMS:0.6%Mn^{4+} phosphors and the absorption spectrum of phytochrome P_{FR}. An obvious spectral overlap existed between the emission band of BLMS:0.6%Mn^{4+} phosphors and the absorption of phytochrome P_{FR}. Furthermore, the IQE of BLMS:0.6%Mn^{4+} sample could be calculated using the following equation:[32]

$$\eta = \frac{\int L_S}{\int E_R - \int E_S} \tag{6}$$

where η is IQE, L_S represents the emission spectrum of the sample, E_S and E_R correspond to the spectra of excitation light with sample and only with $BaSO_4$ reference, respectively. Thus, as shown in Fig. 5(b), the IQE of BLMS:0.6%Mn^{4+} sample was measured to be about 83%, which was much higher than that of many previously reported Mn^{4+}-activated perovskite-type red-emitting phosphors such as Li_2MgZrO_4:Mn^{4+} (IQE: 32.3%), Ba_2YNbO_6:Mn^{4+} (IQE: 29.2%), $NaLaMgWO_6$:Mn^{4+} (IQE: 60%), and $LiLaMgWO_6$:Mn^{4+} (IQE: 69.1%).[2,31,65,66]

Moreover, we also compared our as-prepared BLMS:0.6% Mn^{4+} with some recent reported Mn^{4+}-doped red phosphors for plant growth lighting. Table 1 summarizes their host materials, optimal Mn^{4+} doping concentrations, PL and PLE peaks and IQEs. Clearly, compared to other phosphors, our BLMS:0.6% Mn^{4+} phosphors had higher IQE and good PL properties. These results further demonstrated the excellent optical properties of the as-prepared BLMS:0.6%Mn^{4+} phosphors towards application in plant growth LEDs.

Finally, we fabricated a far-red LED device by coating the BLMS:0.6%Mn^{4+} phosphors onto the surface of a 365 nm near-UV LED chip. The electroluminescence (EL) spectrum of the corresponding LED device under 120 mA driven current was demonstrated in Fig. 5(c). As can be seen, an intense narrow far-red emission band peaking at 700 nm was presented. The CIE coordinates of the device emission were determined to be (0.7199, 0.2800), as shown in Fig. 5(d). These results showed that the as-prepared BLMS:Mn^{4+} phosphors could be promising far-red-emitting phosphors for far-red LEDs applications towards indoor plant growth lighting.

4. Conclusions

In summary, a series of novel Mn^{4+}-activated BLMS far-red-emitting phosphors, which could be excited by UV or blue light, have been successfully prepared by a conventional high-temperature solid-state method. Under UV light excitation at 340 nm, the BLMS:Mn^{4+} phosphors gave rise to an intense far-red emission band peaking at 700 nm due to the $^2E_g \rightarrow {}^4A_{2g}$ transition of Mn^{4+} ions, which could match well with the absorption spectra of phytochrome P_{FR}. The optimal doping concentration of Mn^{4+} ions was determined to be 0.6 mol%, and the concentration quenching mechanism was the nonradiative energy transfer among the nearest-neighbor Mn^{4+} activators in the BLMS host. The CIE chromaticity coordinates of BLMS:0.6% Mn^{4+} sample were measured to be (0.7231, 0.2768). Furthermore, thermal stability was investigated by temperature-dependent emission spectra and the configuration coordinate diagram of Mn^{4+} ions. Finally, we fabricated a bright far-red LED device by coating the BLMS:0.6%Mn^{4+} phosphors onto the surface of a 365 nm near-UV LED chip. These results indicated the BLMS:Mn^{4+} red-emitting phosphors could be applied to obtain far-red LEDs for plant growth lighting.

Conflicts of interest

There are no conflicts to declare.

Acknowledgements

This work was supported by the National Natural Science Foundation of China (No. 51502190), the Program for the Outstanding Innovative Teams of Higher Learning Institutions of Shanxi, and the Open Fund of the State Key Laboratory of Luminescent Materials and Devices (South China University of Technology, No. 2017-skllmd-01).

References

1 Y. Jin, Y. Hu, H. Wu, H. Duan, L. Chen, Y. Fu, G. Ju, Z. Mu and M. He, *Chem. Eng. J.*, 2016, **288**, 596–607.

Open Access Article. Published on 24 January 2019. Downloaded on 1/12/2026 1:20:46 PM.
This article is licensed under a Creative Commons Attribution-NonCommercial 3.0 Unported Licence.

2 A. Fu, Q. Pang, H. Yang and L. Zhou, *Opt. Mater.*, 2017, **70**, 144–152.
3 G. Jiang, B. Yang, G. Zhao, Y. Liu, J. Zou, H. Sun, H. Ou, Y. Fang and J. Hou, *Opt. Mater.*, 2018, **83**, 93–98.
4 L. Huang, Y. Liu, J. Yu, Y. Zhu, F. Pan, T. Xuan, M. G. Brik, C. Wang and J. Wang, *ACS Appl. Mater. Interfaces*, 2018, **10**, 18082–18092.
5 J. Zhong, D. Chen, S. Yuan, M. Liu, Y. Yuan, Y. Zhu, X. Li and Z. Ji, *Inorg. Chem.*, 2018, **57**, 8978–8987.
6 X. Huang, *Nat. Photonics*, 2014, **8**, 748–749.
7 Y. Q. Li, N. Hirosaki, R. J. Xie, T. Takeda and M. Mitomo, *Chem. Mater.*, 2008, **20**, 6704–6714.
8 D. Cui, Q. Xiang, Z. Song, Z. Xia and Q. Liu, *J. Mater. Chem. C*, 2016, **4**, 7332–7338.
9 X. Huang, S. Wang, B. Li, Q. Sun and H. Guo, *Opt. Lett.*, 2018, **43**, 1307–1310.
10 Q. Bai, Z. Wang, P. Li, T. Li, S. Xu and Z. Yang, *Luminescence*, 2016, **31**, 1277–1282.
11 C. Xia, C. Yu, M. Cao, J. Xia, D. Jiang, G. Zhou, D. Zhang and H. Li, *Ceram. Int.*, 2018, **44**, 21040–21046.
12 X. Pu, D. Zhang, H. Li, S. I. Kim, P. Cai, C. Chen and H. J. Seo, *Phys. B*, 2015, **472**, 41–44.
13 L. Li, D. Zhang, X. Pu, J. Zhao, D. Li, C. Wang, S. Wu and T. Ge, *Adv. Powder Technol.*, 2011, **22**, 553–556.
14 J. Zhong, Y. Peng, D. Chen, M. Liu, X. Li, Y. Zhu and Z. Ji, *J. Mater. Chem. C*, 2018, **6**, 13305–13315.
15 Y. Zhu, L. Cao, M. G. Brik, X. Zhang, L. Huang, T. Xuan and J. Wang, *J. Mater. Chem. C*, 2017, **5**, 6420–6426.
16 S. Adachi, *J. Lumin.*, 2018, **197**, 119–130.
17 S. Adachi, *J. Lumin.*, 2018, **202**, 263–281.
18 H.-D. Nguyen, C. C. Lin, M.-H. Fanga and R.-S. Liu, *J. Mater. Chem. C*, 2014, **2**, 10268–10272.
19 M. Kim, W. B. Park, J.-W. Lee, J. Lee, C. H. Kim, S. P. Singh and K.-S. Sohn, *Chem. Mater.*, 2018, **30**, 6936–6944.
20 R. Cao, X. Liu, K. Bai, T. Chen, S. Guo, Z. Hu, F. Xiao and Z. Luo, *J. Lumin.*, 2018, **197**, 169–174.
21 J. Zhong, S. Zhou, D. Chen, J. Li, Y. Zhu, X. Li, L. Chen and Z. Ji, *Dalton Trans.*, 2018, **47**, 8248–8256.
22 F. Xue, Y. Hu, L. Chen, H. Wu, G. Ju, T. Wang and L. Yang, *Ceram. Int.*, 2017, **43**, 15141–15145.
23 S. Liang, M. Shang, H. Lian, K. Li, Y. Zhang and J. Lin, *J. Mater. Chem. C*, 2016, **4**, 6409–6416.
24 X. Ding, Q. Wang and Y. Wang, *Phys. Chem. Chem. Phys.*, 2016, **18**, 8088–8097.
25 D. Kim, S. Park, B. C. Choi, S. H. Park, J. H. Jeong and J. H. Kim, *Mater. Res. Bull.*, 2018, **97**, 115–120.
26 H. Chen, H. Lin, Q. Huang, F. Huang, J. Xu, B. Wang, Z. Lin, J. Zhou and Y. Wang, *J. Mater. Chem. C*, 2016, **4**, 2374–2381.
27 S. Wang, Q. Sun, B. Devakumar, L. Sun, J. Liang and X. Huang, *RSC Adv.*, 2018, **8**, 30191–30200.
28 K. Sankarasubramanian, B. Devakumar, G. Annadurai, L. Sun, Y.-J. Zeng and X. Huang, *RSC Adv.*, 2018, **8**, 30223–30229.
29 Q. Sun, S. Wang, B. Li, H. Guo and X. Huang, *J. Lumin.*, 2018, **203**, 371–375.
30 J. Liang, L. Sun, B. Devakumar, S. Wang, Q. Sun, H. Guo, B. Li and X. Huang, *RSC Adv.*, 2018, **8**, 31666–31672.
31 R. Cao, Z. Shi, G. Quan, T. Chen, S. Guo, Z. Hu and P. Liu, *J. Lumin.*, 2017, **188**, 577–581.
32 X. Huang and H. Guo, *Dyes Pigm.*, 2018, **152**, 36–42.
33 Z. Zhou, J. Zheng, R. Shi, N. Zhang, J. Chen, R. Zhang, H. Suo, E. M. Goldys and C. Guo, *ACS Appl. Mater. Interfaces*, 2017, **9**, 6177–6185.
34 Y. Zheng, H. Zhang, H. Zhang, Z. Xia, Y. Liu, M. S. Molokeev and B. Lei, *J. Mater. Chem. C*, 2018, **6**, 4217–4224.
35 J. Xiang, J. Chen, N. Zhang, H. Yao and C. Guo, *Dyes Pigm.*, 2018, **154**, 257–262.
36 Z. Lu, T. Huang, R. Deng, H. Wang, L. Wen, M. Huang, L. Zhou and C. Yao, *Superlattices Microstruct.*, 2018, **117**, 476–487.
37 A. Fu, A. Guan, D. Yu, S. Xia, F. Gao, X. Zhang, L. Zhou, Y. Li and R. Li, *Mater. Res. Bull.*, 2017, **88**, 258–265.
38 A. Fu, C. Zhou, Q. Chen, Z. Lu, T. Huang, H. Wang and L. Zhou, *Ceram. Int.*, 2017, **43**, 6353–6362.
39 K. Li, H. Lian and R. V. Deun, *J. Lumin.*, 2018, **198**, 155–162.
40 L. Wang, Q. Liu, K. Shen, Q. Zhang, L. Zhang, B. Song and C. Wong, *J. Alloys Compd.*, 2017, **696**, 443–449.
41 L. Li, W. Chang, W. Chen, Z. Feng, C. Zhao, P. Jiang, Y. Wang, X. Zhou and A. Suchocki, *Ceram. Int.*, 2017, **43**, 2720–2729.
42 Y. Takeda, H. Kato, M. Kobayashi, S. Nozawa, H. Kobayashi and M. Kakihana, *J. Phys. Chem. C*, 2017, **121**, 18837–18844.
43 A. M. Srivastava, H. A. Comanzo, D. J. Smith, J. W. Choi, M. G. Brik, W. W. Beers and S. A. Payne, *J. Lumin.*, 2019, **206**, 398–402.
44 G. Zhou, X. Jiang, J. Zhao, M. Molokeev, Z. Lin, Q. Liu and Z. Xia, *ACS Appl. Mater. Interfaces*, 2018, **10**, 24648–24655.
45 C. Yang, Z. Zhang, G. Hu, R. Cao, X. Liang and W. Xiang, *J. Alloys Compd.*, 2017, **694**, 1201–1208.
46 G. Hu, X. Hu, W. Chen, Y. Cheng, Z. Liu, Y. Zhang, X. Liang and W. Xiang, *Mater. Res. Bull.*, 2017, **95**, 277–284.
47 Y. Chen, K. Wu, J. He, Z. Tang, J. Shi, Y. Xu and Z. Liu, *J. Mater. Chem. C*, 2017, **5**, 8828–8835.
48 W. Lu, W. Lv, Q. Zhao, M. Jiao, B. Shao and H. You, *Inorg. Chem.*, 2014, **53**, 11985–11990.
49 R. Cao, W. Luo, H. Xu, Z. Luo, Q. Hu, T. Fu and D. Peng, *Opt. Mater.*, 2016, **53**, 169–173.
50 U. B. Humayoun, S. N. Tiruneh and D.-H. Yoon, *Dyes Pigm.*, 2018, **152**, 127–130.
51 Q. Peng, R. Cao, Y. Ye, S. Guo, Z. Hu, T. Chen and G. Zheng, *J. Alloys Compd.*, 2017, **725**, 139–144.
52 L. Qin, S. Bi, P. Cai, C. Chen, J. Wang, S. I. Kim, Y. Huang and H. J. Seo, *J. Alloys Compd.*, 2018, **755**, 61–66.
53 H. Guo and X. Huang, *J. Alloys Compd.*, 2018, **764**, 809–814.
54 W. Chen, Y. Cheng, L. Shen, C. Shen, X. Liang and W. Xiang, *J. Alloys Compd.*, 2018, **762**, 688–696.
55 S. Zhang, Y. Hu, H. Duan, Y. Fu and M. He, *J. Alloys Compd.*, 2017, **693**, 315–325.
56 S. Zhang, Y. Hu, H. Duan, L. Chen, Y. Fu, G. Ju, T. Wang and M. He, *RSC Adv.*, 2015, **5**, 90499–90507.
57 J. Zhong, X. Chen, D. Chen, M. Liu, Y. Zhu, X. Li and Z. Ji, *J. Alloys Compd.*, 2019, **773**, 413–422.
58 Q. Shao, H. Ding, L. Yao, J. Xu, C. Liang and J. Jiang, *RSC Adv.*, 2018, **8**, 12035–12042.

Open Access Article. Published on 24 January 2019. Downloaded on 1/12/2026 1:20:46 PM.
This article is licensed under a Creative Commons Attribution-NonCommercial 3.0 Unported Licence.

59 H. Deng, Z. Gao, N. Xue, J. H. Jeong and R. Yu, *J. Lumin.*, 2017, **192**, 684–689.
60 X. Huang and H. Guo, *RSC Adv.*, 2018, **8**, 17132–17138.
61 B. Li, S. Wang, Q. Sun, C. Lu, H. Guo and X. Huang, *Dyes Pigm.*, 2018, **154**, 252–256.
62 Z. Lu, A. Fu, F. Gao, X. Zhang and L. Zhou, *J. Lumin.*, 2018, **203**, 420–426.
63 G. Annadurai, B. Devakumar, H. Guo, R. Vijayakumar, B. Li, L. Sun, X. Huang, K. Wang and X. W. Sun, *RSC Adv.*, 2018, **8**, 23323–23331.
64 J. Liang, P. Du, H. Guo, L. Sun, B. Li and X. Huang, *Dyes Pigm.*, 2018, **157**, 40–46.
65 J. Liang, L. Sun, B. Devakumar, S. Wang, Q. Sun, H. Guo, B. Li and X. Huang, *RSC Adv.*, 2018, **8**, 27144–27151.
66 X. Huang, J. Liang, B. Li, L. Sun and J. Lin, *Opt. Lett.*, 2018, **43**, 3305–3308.
67 L. Shi, Y.-j. Han, H.-x. Wang, D.-c. Shi, X.-y. Geng and Z.-w. Zhang, *J. Lumin.*, 2019, **208**, 307–312.
68 L. Shi, Y.-j. Han, Z.-g. Zhang, Z.-x. Ji, D.-c. Shi, X.-y. Geng, H. Zhang, M. Li and Z.-w. Zhang, *Ceram. Int.*, 2018, DOI: 10.1016/j.ceramint.2018.11.166.
69 L. Shi, Y.-j. Han, Z.-x. Ji and Z.-w. Zhang, *J. Mater. Sci.: Mater. Electron.*, 2019, DOI: 10.1007/s10854-018-00590-5.
70 L. Shi, J.-x. Li, Y.-j. Han, W.-l. Li and Z.-w. Zhang, *J. Lumin.*, 2019, **208**, 201–207.
71 R. Cao, T. Chen, Y. Ren, T. Chen, H. Ao, W. Li and G. Zheng, *J. Alloys Compd.*, 2019, **780**, 749–755.
72 Q. Sun, S. Wang, B. Devakumar, B. Li, L. Sun, L. Jia, D. Chen and X. Huang, *RSC Adv.*, 2018, **8**, 39307–39313.
73 L. Li, Y. Pan, Z. Chen, S. Huang and M. Wu, *RSC Adv.*, 2017, **7**, 14868–14875.

 This journal is © The Royal Society of Chemistry 2019